Journal of Geoscience and Environment Protection, 2023, 11, 268-296
https://www.scirp.org/journal/gep
ISSN Online: 2327-4344
ISSN Print: 2327-4336

Characterization of Near Surface Intrusions in South-West Cameroon Zone Using Gravity Data: Mining and Geothermal Implications

Ghislain Nkamgan Ndongmo[1,2], Fidèle Koumetio[1,2*], François Ngapgue[2], Ernest Léontin Lemoubou[2]

[1]Laboratory of Environmental Physics, Faculty of Sciences, University of Dschang, Dschang, Cameroon
[2]Research Unit of Mechanics and Physical Systems Modeling (UR-2MSP), Department of Physics, Faculty of Sciences, University of Dschang, Dschang, Cameroon
Email: *koumetiof@yahoo.fr, *fidele.koumetio@univ-dschang.org

How to cite this paper: Ndongmo, G. N., Koumetio, F., Ngapgue, F., & Lemoubou, E. L. (2023). Characterization of Near Surface Intrusions in South-West Cameroon Zone Using Gravity Data: Mining and Geothermal Implications. *Journal of Geoscience and Environment Protection, 11,* 268-296.
https://doi.org/10.4236/gep.2023.119018

Received: August 3, 2023
Accepted: September 23, 2023
Published: September 26, 2023

Abstract

The succession of tectonic phenomena in the South-West Cameroon area suggests that structures from the upper mantle infiltrated and took advantage of the cracks and fractures left by these phenomena to get closer to the earth's surface. However, the intrusive structures closest to the surface remain poorly known. The objective of this work is to improve the knowledge related to the interpretation of gravity data in order to characterise the near-surface intrusive bodies in the South-West Cameroon area, and then analyse their mining and geothermal implications. To achieve this objective, the indirect, inverse and normalized standard deviation (NSTD) methods were used. The NSTD method was used to detect the contours of the intrusive bodies. The indirect method (spectral analysis) was used to determine the depths of the interfaces of three intrusive bodies, one located on the Bipindi-Ebolowa I axis (G5), the other on the Eseka-Pouma axis (G8) and the last on the Bokito-Monatele axis (G11). The results obtained show roofs located between 0 and 0.61 km, between 0 and 0.37 km and between 0 and 0.73 km for the G5, G8 and G11 bodies, respectively. Finally, the application of the 2D inversion method allowed us to estimate the density contrasts of the intrusive bodies (G5, G8 and G11). The superposition of the intrusive bodies detected by the NSTD with the geological and mineral resources map, as well as an analysis of the results obtained, gave indications of interesting zones for mining prospecting and for the search for geothermal reservoirs.

Keywords

Bouguer Anomaly, Spectral Analysis, Inverse Method, NSTD Method, Intrusive Body

1. Introduction

The area of South-West Cameroon, the subject of this study, is located between 2˚24' - 4˚39' North latitude and 9˚59' - 11˚31' East longitude. Several geological formations are found in the South-West Cameroon area, which were formed by erosion phenomena or by magmatic storage from which charnockites and an assemblage of basic and ultrabasic rocks were derived (Maurizot et al., 1986; Bonda et al., 2022; Shanel et al., 2022). Among others, one can cite the greenstone formations located between Lolodorf-Ngomezap that remain in a relict state within the intrusive granitoïds of the Nyong unit and that present basic facies including ortho amphibolites derived from the transformation of dolerites (Tchameni, 1997). This area is also crossed by several tectonic structures such as the Sanaga fault which is an extension of the Kribi-Campo fault (Ngako et al., 2003) as well as the deep faults f2 and f31 (**Figure 1**) highlighted by Koumetio (2004). The study area is also host to several intrusive bodies that were highlighted using the multiscale analysis of maxima of the horizontal derivative of the vertical gradient of the Bouguer anomaly and whose depths are relatively large since the contours of these bodies were obtained after an upward extension that eliminates the effects of superficial structures (Koumetio et al., 2012, 2014; Koumetio, 2017). During petrographic studies and structural analyses, mylonitic metagranodiorite rocks have been highlighted on the Kribi-Campo shear by Kouankap et al. (2018).

It then appears that these previous works did not make it possible to locate the intrusive bodies situated near the surface layer of the study area. However, it should be noted that very often, deposits such as metals are generated by magmas that rise to the surface through faults; exploitable hot sources (or geothermal reservoirs) may also be due to these magmas that have migrated towards the earth's surface. These magmatic upwellings influence the density model, linked to the gravity anomaly data measured at the surface, which remains poorly known and which can be an asset for orientation in mining exploration and the search for geothermal reservoirs. It is, therefore, important to ask questions about the magnitude and structuring of near-surface magmatic stocks.

The objective of this work is to improve the knowledge related to the interpretation of gravity data in order to characterize the near-surface intrusive bodies in the South-West Cameroon area, and then analyse their mining and geothermal implications. To achieve this objective, we will first apply the normalized standard deviation method (NSTD) on residual anomaly maps that generally show the effects of near-surface structures. Then, we propose to apply the spectral analysis method on these residual anomalies, to characterize the interfaces of the surface structures detected by NSTD. Finally, we will apply the 2D inversion method based on the formulation of Last and Kubik (1983) to give an estimate of the density distribution and the extent of the causal bodies obtained by the normalized standard deviation (NSTD).

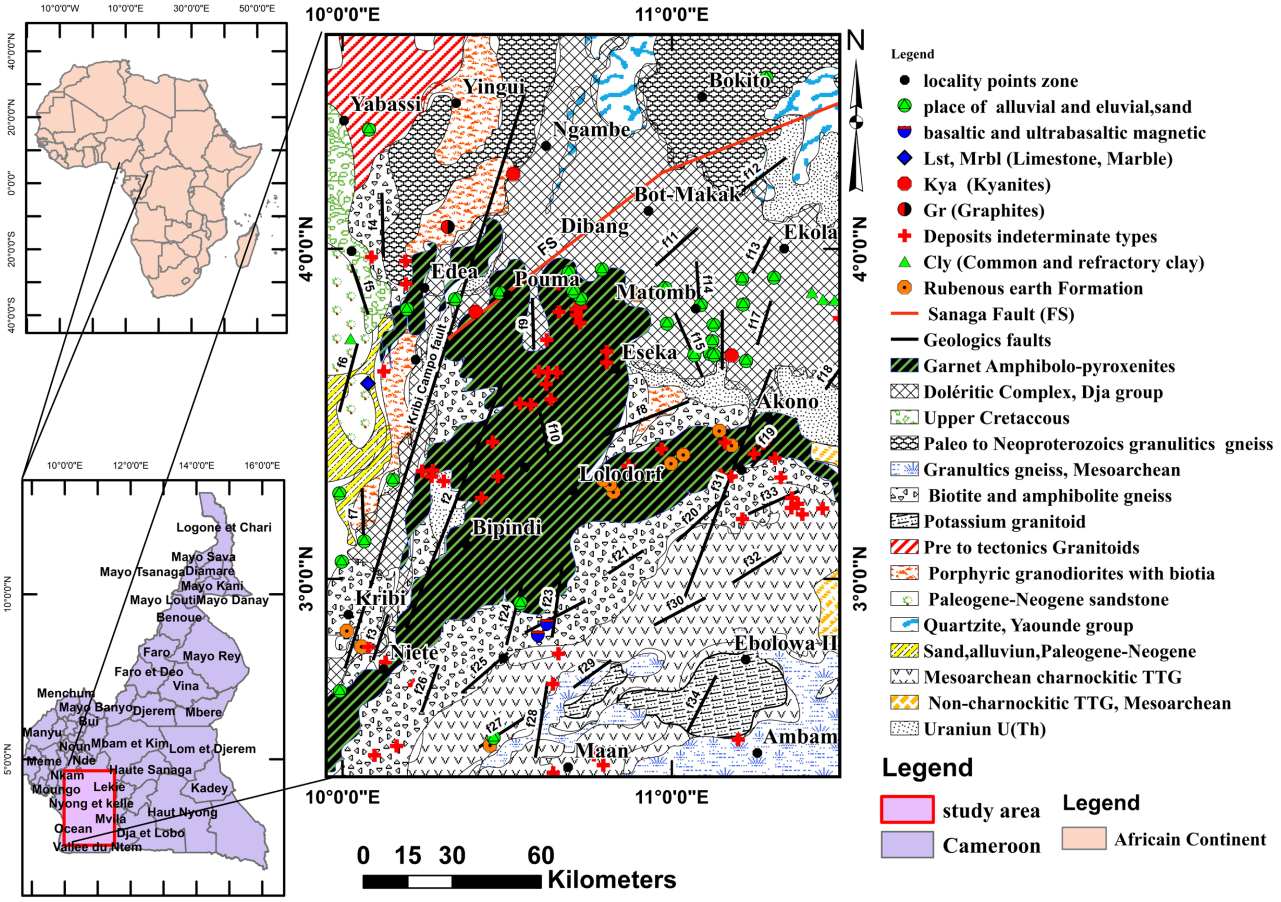

Figure 1. Geological and location map of southwest Cameroon (modified by Maurizot et al., 1986; Nedelec et al., 1990; Feybesse et al., 1998; Nsifa, 2005; Toteu et al., 2008; Nzenti et al., 2011).

2. Geological and Tectonic Setting

The study area consists mainly of formations from the Nyong unit. This unit corresponds to the remobilised north-western edge of the Ntem Complex (Maurizot et al., 1986; Minyem & Nedelec, 1990; Tchameni, 1997). According to Maurizot et al. (1986), fault deformation was responsible for the development of blastomylonite shear zones, which appear irregularly throughout the Nyong and Ntem units. Part of the study area lies within the Yaounde Group of the southern Cameroon domain. The Yaounde Group comprises several series, generally consisting of Neoproterozoic volcano-sedimentary formations straddling the Congo Craton (Nzenti, 1998). Tabod (1991) studied the volcanic line of Cameroon in its continental south-western part and found that the earthquakes that occurred in the vicinity of Kribi had foci located at a depth of more than 30 km.

In this area, Koumetio (2004) highlights two SSW-NNE-trending normal faults, one running along the Edea-Kribi axis and the other along the Eseka-Akom II axis with vertical displacements of around 20 km (faults f2 and f31 in **Figure 1**). Among the faults that cross our study area, the Sanaga fault, which intercepts the north-western geophysical boundary of the Congo craton, has been highlighted

and interpreted by Tchameni et al. (2006) as an extension of the Kribi-Campo fault. This fault appears to have the same characteristics as the offshore fault system known as the Kribi fracture zone (Owono, 2010). Tokam (2010) used seismological data to propose the average depth of the Moho, indicating that it is about 45 km below the craton and about 28 km below the Kribi-Campo domain. This author showed that the entire lower crust is made up of basic-type rocks. Owona Angue et al. (2011) carried out geophysical work and proposed a gravity model along a profile extending from Kribi to Lolordorf. They have shown that above the lower crust, there are several other structures making up the upper crust: Syenite (Pan-African), Granulites (Pan-African), part of the Nyong Unit (Eburnian), Ntem Granite (Congo Craton), Granitoid Greenstone, Gneiss (Craton) and Phanerozoic Cover (Loose & Schenk, 2018; Bouyo Houketchang et al., 2019; Nga Essomba et al., 2020; Owona et al., 2021a, 2021b; Mvodo et al., 2022).

None of these studies show discontinuity zones related to the boundaries of near-surface intrusive bodies. They highlight intrusive bodies located at great depths and, for many of them, do not specify whether they could extend to a depth close to the surface. Identifying the intrusive bodies closer to the surface that contribute to the observed gravity anomaly would be an asset for mining and geothermal research.

3. Data Origin and Processing

The gravity data used in this work were collected during gravity surveys of Central Africa by ORSTOM, and supplemented by survey data from Princeton University in 1968, the University of Leeds in 1982, IRGM and the University of Leeds between 1984 and 1988, referenced respectively by Collignon (1968) and Poudjom-Djomani et al. (1996). The measurement campaigns were carried out by car, along accessible roads. For the measurements carried out by ORSTOM, the inter-station distances were 3 km, while those carried out by the other organisations were between 4 and 10 km. Gravity measurements were made using the Lacoste & Romberg (model G, n˚ 471 and 823), Worden (n˚ 69, 135, 313, 600 and 1153), World Wide (n˚ 36), Canadian Scintrex (n˚ 305G) and North-American (n˚ 124 and 165) gravimeters.

In order to standardize all the gravity surveys, the Bouguer anomalies were recalculated in the international reference system IGSN71 (Gantar et al., 1971). The compilation of all the gravity surveys carried out in our study area led to 421 measurement points shown in **Figure 5**.

The values of the simple Bouguer anomaly were obtained after drift, free air and Bouguer corrections had been made. To obtain the Bouguer anomaly values used in this work, we performed the terrain correction on the data in the Oasis Montaj software, taking an average density of the earth's crust equal to 2.67 g/cm^3.

4. Methods

To better interpret the Bouguer anomalies obtained, different techniques were

applied: the regional-residual separation method, the normalized standard deviation (NSTD), spectral analysis, and 2D inversion.

4.1. Regional-Residual Separation

The separation of the residual field from the regional field is highly dependent on the regional field (Vigneresse, 1990; Koumetio et al., 2019), the choice of which requires a good knowledge of the geology of the study region. The choice of the regional field determines the nature and appearance of the residual. This separation will be done by the polynomial method, because of its flexibility and its ability to highlight anomalies of various extensions. If B represents the Bouguer anomaly, it can be considered as the sum of two terms Reg and Res such that:

$$B = Reg + Res \tag{1}$$

where Reg represents the regional anomaly and Res the residual anomaly. The regional anomaly, because of its origin, must be as regular as possible, i.e. the curvature of the surface representing it must be small. We will focus our attention on the residual anomalies. The formula governing this separation is obtained as follows. Let $g(x_i; y_i)$, the value of the Bouguer anomaly at point p_i, it is a matter of computing the values of the regional $Reg(x_i; y_i)$ and that of the residual $Res(x_i; y_i)$, by a suitable choice of the polynomial $F(x_i; y_i)$ of order n; this polynomial generates an analytical surface $Reg(x_i; y_i)$ as close as possible to the experimental surface $g(x_i; y_i)$. According to Radhakrishna and Krishnamacharyulu (1990), this polynomial can be put in the form:

$$F_n(x_i; y_i) = Bi + \sum_{j=1}^{n} \sum_{L=0}^{j} B_m A_m(x_i; y_i) \tag{2}$$

where $A_m = x_i^L y_i^{(j-L)}$, B_m are the coefficients to be determined, $m = \frac{j(j+3)}{2} - L + 1$ with the maximum value of m being $1/2(n+1)(n+2)$. The difference between the homologous points of the experimental and analytical surfaces respectively is designated by:

$$\varepsilon = g(x_i; y_i) - F_n(x_i; y_i) \tag{3}$$

The number of stations p_i where the Bouguer anomaly $g(x_i, y_i)$ is known, is n_0. The adjustment of the analytical surfaces consists in minimizing the quadratic deviation of Equation (4):

$$E = \sum_{i=1}^{n_0} \varepsilon_i^2 \tag{4}$$

Let $\partial E / \partial B_k = 0$ with $1 \le k \le m$. Determining the coefficients B_m requires the solution of a system of m equations. Once the coefficient B_m is determined, the analytical residual is calculated by the relation:

$$Res_n(x_i; y_i) = g(x_i; y_i) - F_n(x_i; y_i) \tag{5}$$

When the degree of the polynomial is small, the regional anomaly has relatively large deviation values compared to the Bouguer anomaly. As we increase

the order of the polynomial, the regional anomaly becomes closer to the total anomaly, which allows us to highlight the structures closer to the surface with the corresponding residual anomalies.

The highlighting of intrusive bodies will be done by exploiting the residual anomalies of order 1 and 7 for several reasons:

- Koumetio et al. (2019) have shown that credible analyses of the subsurface structures of the South West-Cameroon region can be made using the residual anomaly maps of order 1 to 8.
- The highlighting of the closest structures to the surface that have an effect on the Bouguer anomaly is done by exploiting the highest order residual anomaly map but to avoid a level of noise that could be annoying in the 8th order residual, the 7th order has been chosen.
- If some intrusive bodies detected from the 7th order residual anomalies are also highlighted by using the 1st order residual anomalies, then this work would gain a lot of credibility since the noise level is very low on the 1st order residual compared to what the 7th order may present.

4.2. Upward Continuation

The upward continuation is an operator that acts as a low pass filter by attenuating the high frequencies of a signal. Let $g(x,y,z)$ be a function defined in three-dimensional space. Let us decompose $g(x,y,z)$ in terms of wavelengths λ_x and λ_y along the x and y directions. $G(k_x,k_y,z)$ is its Fourier transform in two dimensions where k_x and k_y are the wavenumbers in the x and y directions, respectively. If the value of the spectrum is known for $z=0$, then its value for $z=h$ is given by the relation (6):

$$G(k_x,k_y,h)=G(k_x,k_y,0)\mathrm{e}^{-h\sqrt{k_x^2+k_y^2}} \tag{6}$$

We, therefore, obtain $g(x,y,h)$ by inverse transformation of $G(k_x,k_y,h)$. An upward continuation to 2 km was performed on the residual anomalies only to reduce the noise level in the data. These upward continuation data were used only to determine the contours of the intrusive bodies using the normalized standard deviation (NSTD) method. The Fourpot program (Pirttijärvi, 2009; Fofie et al., 2019; Kenyo et al., 2023) was used to perform the upward continuation.

4.3. Normalized Standard Deviation (NSTD) Method

The NSTD method allows the identification of discontinuity zones and contours of subsurface structures with greater accuracy than methods such as the Total Horizontal Derivative, Tilt Angle, THDR and Theta Map (Cooper & Cowan, 2008). NSTD is a technique for enhancing fine detail in potential data. The window for calculating the standard deviation norm of an image or gravity map is a simple measure of local variability. Equation (7), applied to the residual anomalies, makes it possible to observe all the discontinuities of superficial origin, whether

weak or strong:

$$\mathrm{NSTD} = \frac{\sigma\left(\frac{\partial g}{\partial z}\right)}{\sigma\left(\frac{\partial g}{\partial x}\right) + \sigma\left(\frac{\partial g}{\partial y}\right) + \sigma\left(\frac{\partial g}{\partial z}\right)} \tag{7}$$

The standard deviations (σ) in Equation (7) are calculated using a 5 × 5 square calculation window of data points, which highlights all locations of the observed data (Cooper & Cowan, 2008). This treatment of gravity maps clearly gives good contour resolution for shallower intrusive structure models.

4.4. Spectral Analysis Method

The spectral analysis technique helps in estimating the depth of major density contrasts, from the energy spectrum of observed gravity anomalies. Spector and Grant (1970) demonstrated that the discrete Fourier transform of a range of N data points distributed over a profile is given by Formula (8):

$$F_k(w) = \frac{1}{N}\sum_{n=1}^{N-1} f(n)\mathrm{e}^{\frac{-2\pi kn}{N}} \tag{8}$$

where $f(n)$ is the value of the residual anomaly considered, n is the order number and k is the wavenumber.

The energy spectrum of the gravity anomalies $E_k(w)$ is defined by relation (9):

$$E_k(w) = \left|F_k(w)\right|^2 \tag{9}$$

The average depth of the source is then estimated by Formula (10) (Dimitriadis et al., 1987):

$$h = \frac{\Delta \ln E(w)}{4\pi\Delta k} \tag{10}$$

4.5. Last and Kubik's 2D Inversion Method

Our model consisted of subdividing the subsurface of our study area into a large number of infinitely long horizontal prisms of rectangular section and unknown density. To illustrate, we start from a 2D model proposed by Last and Kubik (1983) that minimizes the volume of the causal body, using a fixed shape to estimate the physical parameters of the model. This method gives a wide opening to the linear modeling process between the block parameters and the observed data. This will reduce the problems of resulting density distributions in an area. The model shown in **Figure 2** represents the discretization of the subsurface of the study area.

To model the effects illustrated by the gravity data, we started with the vertical component of the gravitational attraction of a two-dimensional body at a position x_j in a Cartesian coordinate system based on Formula (11) presented by Blakely and Simpson (1986).

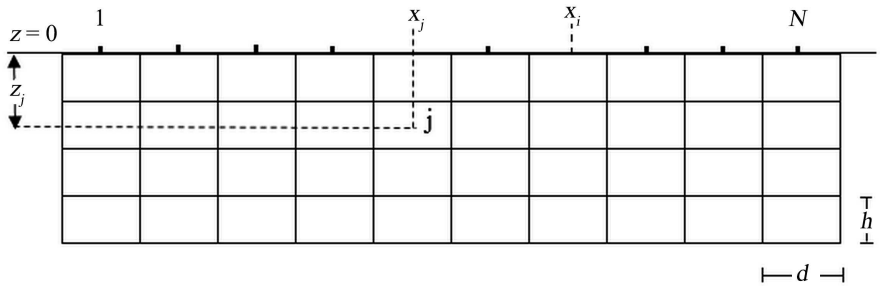

Figure 2. The 2D model showing the number of blocks *j* of data point *i*. *d* and *h* are the horizontal and vertical dimensions of an elementary rectangular block.

$$g_i = 2\gamma\rho_j \iint \frac{\left(z_j \pm h/2\right)\mathrm{d}x\mathrm{d}z}{\left(z_j \pm h/2\right)^2 + \left(x_i - x_j \pm d/2\right)^2} \tag{11}$$

where γ is the universal gravitational constant and ρ is the density, assumed to be constant inside each prism. The y-axis has the direction of the invariant and variations in the densities are only allowed in the directions *x* and *z*. The model is obtained by applying Equation (12) to an isolated prism (**Figure 2**). For this model, the gravity effect at the i^{th} data point for M blocks of homogeneous density is given by:

$$g_i = \sum_{j=1}^{M} a_{ij}\rho_j + e_i, i = 1, \cdots, N \tag{12}$$

with

$$a_{ij} = 2\gamma \iint \frac{\left(z_j \pm h/2\right)\mathrm{d}x\mathrm{d}z}{\left(z_j \pm h/2\right)^2 + \left(x_i - x_j \pm d/2\right)^2} \tag{13}$$

and ρ_j is the density of the j^{th} block, e_i is the noise associated with the i^{th} data point, and a_{ij} represents the elements of the matrix giving the influence of the j^{th} block on the i^{th} gravity value; with $i = 1, \cdots, N$, $j = 1, \cdots, M$, N is the total number of data and M represents the number of blocks constituting the domain.

In order for the direct model to calculate the vertical gravitational anomaly at a point due to the presence of a two-dimensional shaped body, we used an algorithm based on the development made by Last and Kubik (1983). The horizontal and vertical distance between the center of the reference system and the center of the j^{th} rectangular prism (**Figure 3**) are respectively x_j and z_j. *d* and *h* are respectively the width and height of the rectangle. The vertical gravitational anomaly at the i^{th} measurement point due to the whole j^{th} rectangular block can be illustrated as follows.

The exact expression of a_{ij} is obtained (Equation (14)) once the vertical attraction is applied to the four vertices of the j^{th} block (**Figure 3**):

$$\begin{aligned} a_{ij} = 2\gamma\Bigg[&\left(x_i - x_j + \frac{d}{2}\right)\log\left(\frac{r_2 r_3}{r_1 r_4}\right) + d\log\left(\frac{r_4}{r_3}\right) + \left(z_j - h/2\right)\left(\theta_3 - \theta_1\right) \\ &-\left(z_j + h/2\right)\left(\theta_4 - \theta_2\right)\Bigg] \end{aligned} \tag{14}$$

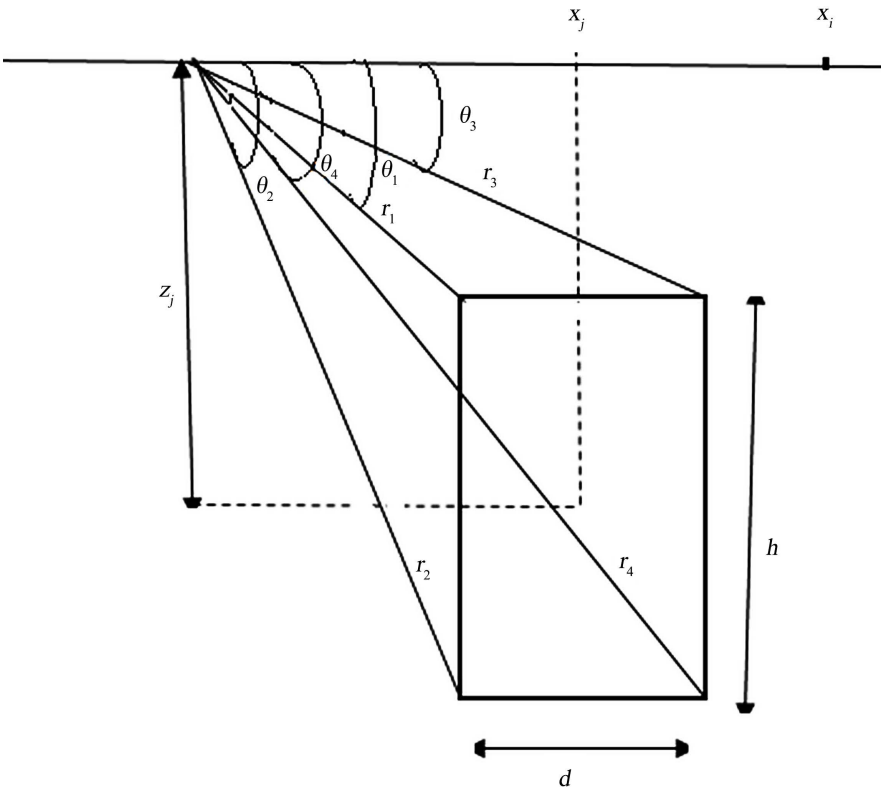

Figure 3. 2D model of an isolated prism.

with

$$\begin{cases} r_1^2 = \left(x_i - x_j + d/2\right)^2 + \left(z_j - h/2\right)^2 \\ r_2^2 = \left(x_i - x_j + d/2\right)^2 + \left(z_j + h/2\right)^2 \\ r_3^2 = \left(x_i - x_j - d/2\right)^2 + \left(z_j - h/2\right)^2 \\ r_4^2 = \left(x_i - x_j - d/2\right)^2 + \left(z_j + h/2\right)^2 \end{cases} \tag{15}$$

$$\begin{cases} \theta_1 = \arctan\left[\left(x_i - x_j + d/2\right)/\left(z_j - h/2\right)\right] \\ \theta_2 = \arctan\left[\left(x_i - x_j + d/2\right)/\left(z_j + h/2\right)\right] \\ \theta_3 = \arctan\left[\left(x_i - x_j - d/2\right)/\left(z_j - h/2\right)\right] \\ \theta_4 = \arctan\left[\left(x_i - x_j - d/2\right)/\left(z_j + h/2\right)\right] \end{cases} \tag{16}$$

The data equation can be written in matrix notation which is the starting equation for the inversion.

$$G = AX + E \tag{17}$$

where G is the observed gravity data matrix, X is the density distribution that explains G, and E is the error due to the data.

Given an observed gravity data set G, an algorithm for modeling the inverse problem would help us find a density distribution X that explains G, provided that the information about the source is a priori sufficient. To avoid the instabil-

ity problem, the algorithm used for the inversion of gravity data must take into account parameterization, measurement and data processing errors. In addition, it must be flexible enough to take into account prior information to avoid the problem associated with non-uniqueness (Zewge et al., 2011). In general, all inversion programs lead to solutions that can be grouped by deterministic approaches. In the deterministic approach, one can assume that a prior density function can be assigned to the model and one tries to solve the problem by maximizing the probability of having a valid model later (Chakravarthi et al., 2002). On the other hand, the deterministic approach assumes that there is no prior information and tries to solve the problem using as much information as possible from the measured data (Zewge et al., 2011).

These approaches try to find a solution that has several local minima, by iterative application to reach a global optimization. To achieve this global optimal value, the density of a rectangular prism was considered as a weighting matrix (W_m) to obtain the compact distribution of the subsurface mass. The inversion procedure converges to a compact model that is not necessarily single-density and most of the time, it yields a high-density model that is not realistic. We will solve the inversion problem using the method of weighted least squares (Last & Kubik, 1983). The formulation is as Equation (18):

$$\bar{X} = W_m^{-1} A\left(AW_m^{-1}A^{\mathrm{T}} + W_e^{-1}\right)^{-1} G \tag{18}$$

where G is the matrix of the observed gravity data, A is the matrix that contains the elements of the vertical gravitational attraction of the j^{th} block with unit density on the i^{th} measurement point, A^{T} is the transpose of the matrix A, $\bar{X}$ is a vector that contains M number of unknown parameters, W_e is the weighting matrix that depends on the density ρ and the noise e at each measured data point. Indirect modeling of gravity data requires iterative numerical procedures of testing and error correction, which in turn are time consuming and difficult for complicated cases.

5. Results

5.1. Maps of the NSTD Corresponding to the First and Seventh Order Residuals

Figure 4 shows the NSTD maps. To obtain these maps, Formula (7) was applied to calculate the normalised standard deviation (NSTD) using the 1st order (**Figure 4(a1)**) and 7th order (**Figure 4(b1)**) residuals anomalies upward continued at 2 km to reduce noise effects on the data. It highlights the boundaries of the near surface structures present in the study area and it can be seen that the effects of the structures are quite distinct, giving a good appreciation of the discontinuities. On these maps, one can see the arrangement in the form of bright ripples. A curvilinear arrangement of ripples indicates the presence of an intrusive body. The contours of these intrusive bodies are shown on the NSTD maps of the 1st (**Figure 4(a2)**) and 7th (**Figure 4(b2)**) order residuals.

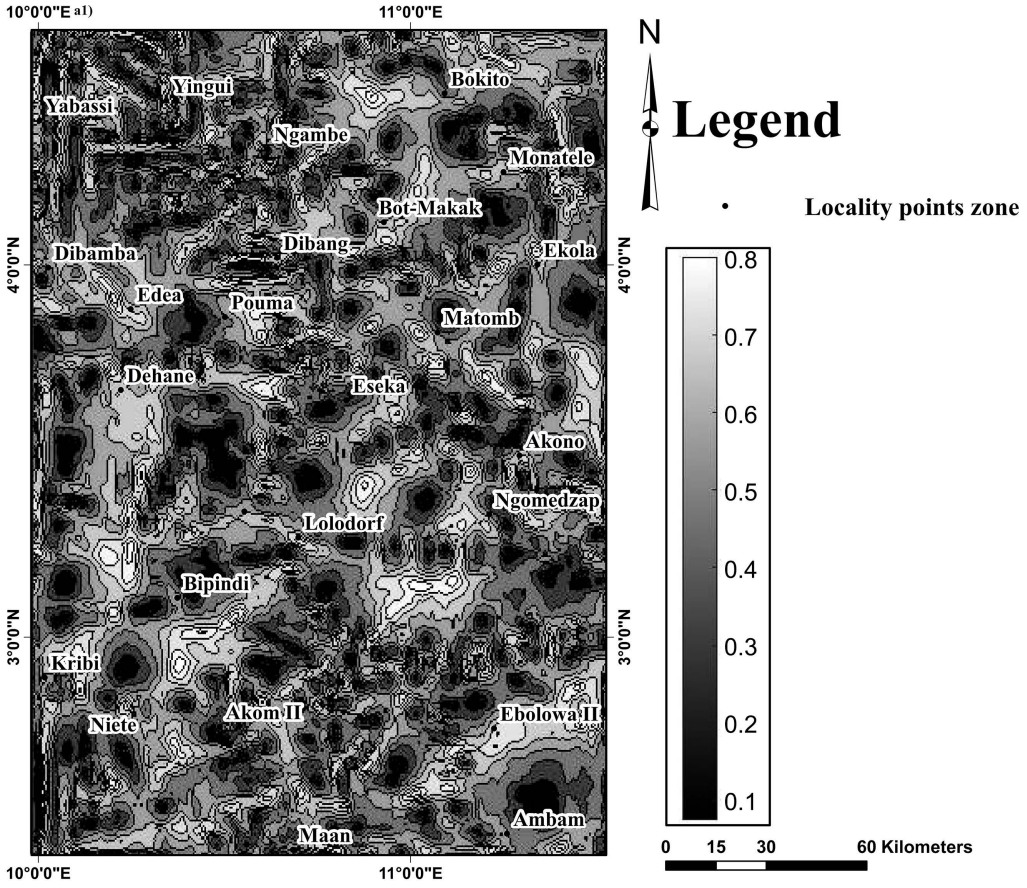
10°0'0"E a1)
11°0'0"E
4°0'0"N
3°0'0"N
Yingui
Bokito
Yabassi
Ngambe
Monatele
Bot-Makak
Dibamba
Dibang
Ekola
Edea
Pouma
Matomb
Dehane
Eseka
Akono
Ngomedzap
Lolodorf
Bipindi
Kribi
Akom II
Niete
Ebolowa II
Ambam
Maan
N
Legend
Locality points zone
0.8
0.7
0.6
0.5
0.4
0.3
0.2
0.1
0 15 30 60 Kilometers

(a1)

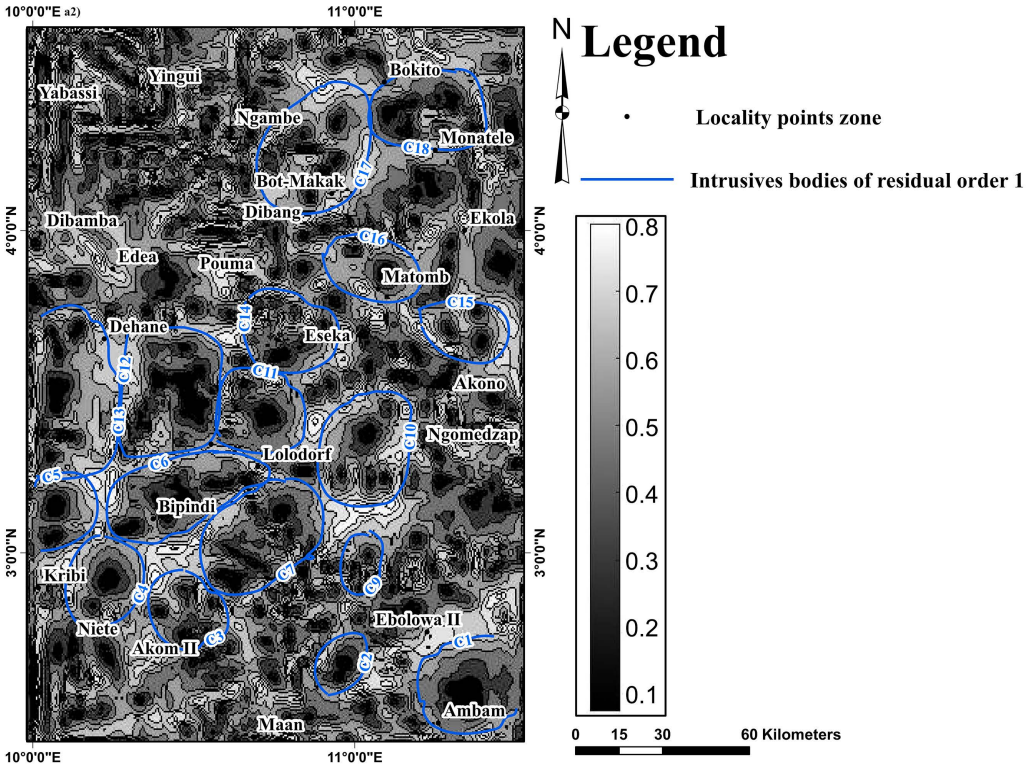
10°0'0"E a2)
11°0'0"E
4°0'0"N
3°0'0"N
Yingui
Bokito
Yabassi
Ngambe
Monatele
C18
C17
Bot-Makak
Dibang
Dibamba
Ekola
C16
Edea
Pouma
Matomb
C15
Dehane
C14
Eseka
C12
C11
Akono
C13
C10
Ngomedzap
Lolodorf
C6
C5
Bipindi
Kribi
C7
C9
C4
Ebolowa II
Niete
C3
Akom II
C1
C2
Ambam
Maan
N
Legend
Locality points zone
Intrusives bodies of residual order 1
0.8
0.7
0.6
0.5
0.4
0.3
0.2
0.1
0 15 30 60 Kilometers

(a2)

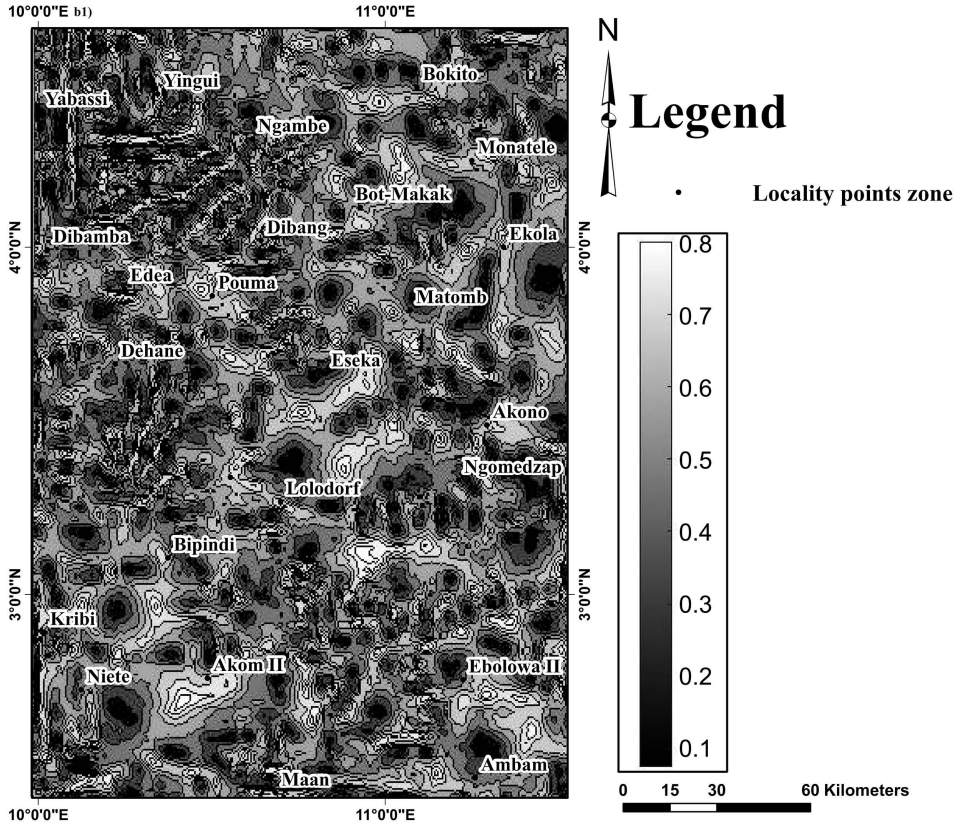

(b1)

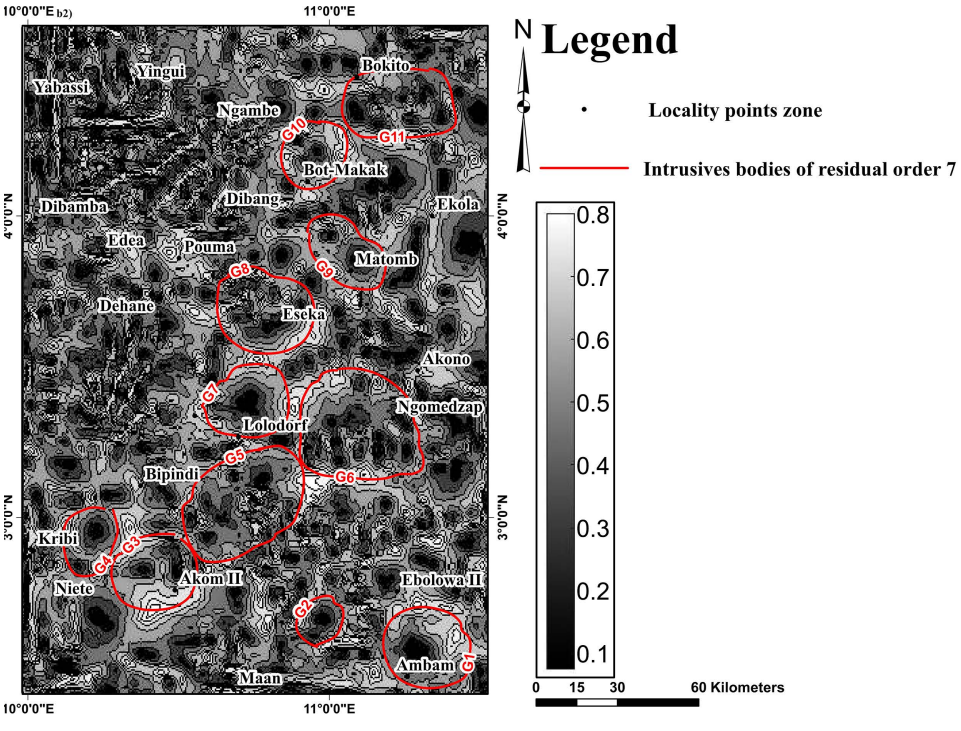

(b2)

Figure 4. NSTD map of the residuals: (a1) of order 1, (b1) of order 7, (a2) of order 1 with materialization of the contours of intrusive bodies, (b2) of order 7 with materialization of the contours of intrusive bodies.

5.2. Overlay of the Maps of Intrusive Bodies Obtained by NSTD of the First and Seventh Order Residuals

Figure 5 shows the intrusive bodies detected by NSTD on the first-order (blue) and seventh-order (red) residuals. The distribution of data points on this map shows that intrusive structures have only been considered in areas where there are measured data points. It can be seen in Figure 5 that some of the contours of the intrusive bodies in blue and red almost overlap (C2 and G2, C7 and G5, C14 and G8, C16 and G9, C18 and G11), which would probably indicate that these bodies extend from the 1st to the 7th order residual. It can also be seen in Figure 5 that some of the blue and red intrusive body contours intermingle (C1 and G1, C3 and G3, C4 and G4, C11 and G7, C17 and G10), indicating in each case that it is either the same body that extends from the 1st to 7th order residual with a lateral surface area that varies with depth, or they are two different bodies. Whether the contours of the intrusive bodies are overlapping or intermingling, their vertical extents can only be determined from the depths of their interfaces, which can be done by spectral analysis

5.3. Overlay of Intrusive Bodies Maps on Residual Anomaly Maps

Figure 6 is a map of the first-order residual superimposed on the intrusive bodies detected by NSTD using the first-order residual anomalies. It can be seen that some of the intrusive bodies obtained by NSTD are superposed on the intrusive bodies that occur on the first order residual by quasi-circular isogals (C1, C5, C6, C13, C17 and C18).

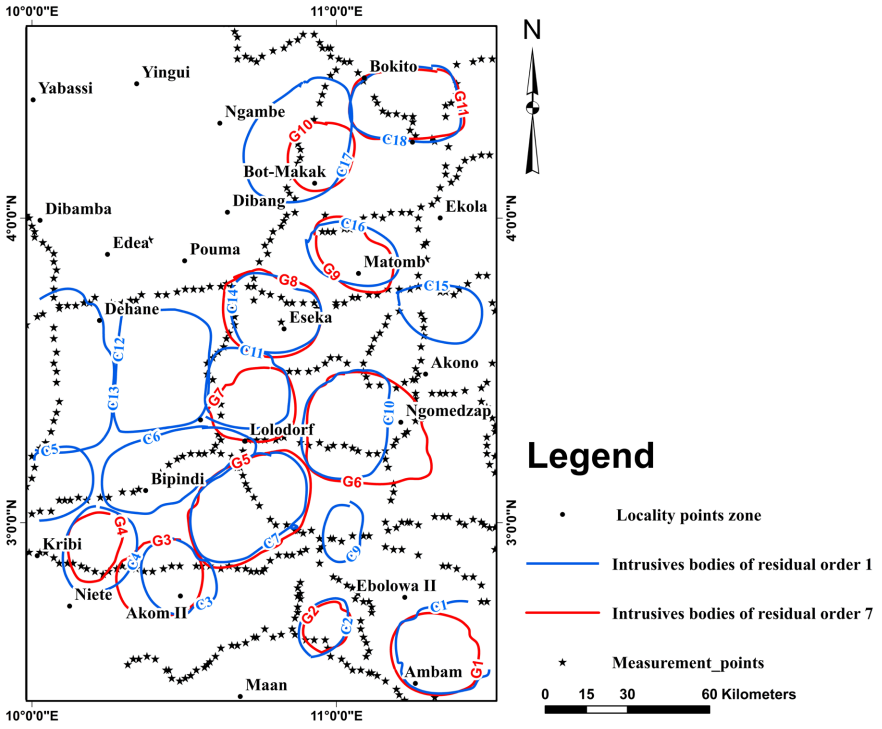

Figure 5. Map of intrusive bodies produced by the NSTD of 1st and 7th order residuals.

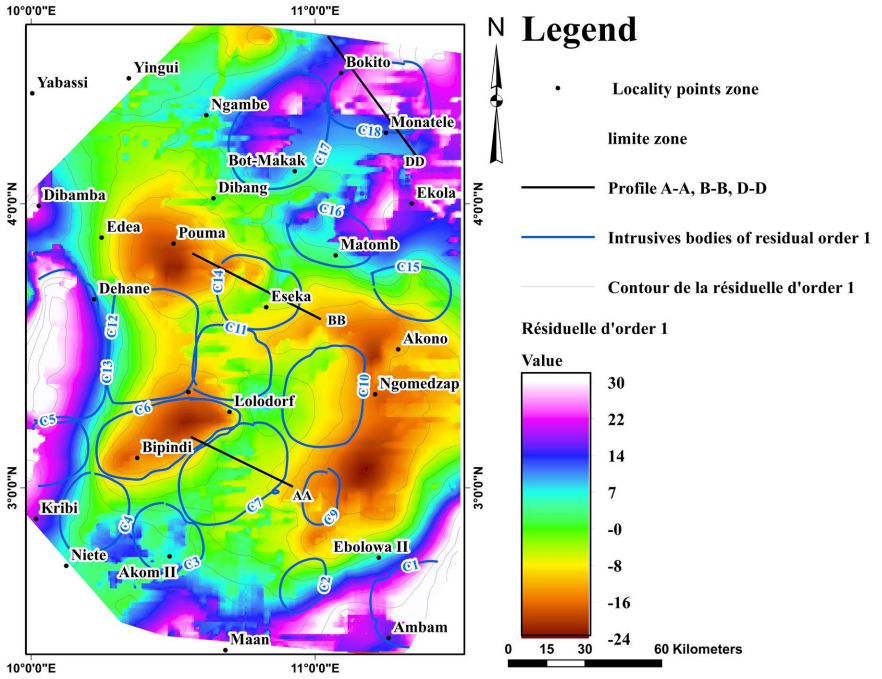

Figure 6. Overlay of the residual of order 1 on the intrusive bodies detected by the NSTD.

Figure 7 is the map of the 7th order residual superimposed on the intrusive bodies detected by NSTD using the 7th order residual anomalies. The same observation can be made about the intrusive bodies obtained by NSTD and which are superimposed on the intrusive bodies presented on the 7th order residual by quasi-circular isogals (G1, G3, G4, G6 and G9).

5.4. Application of Spectral Analysis to AA, BB and DD Profile Data

For the determination of the gravimetric power spectrum, we plotted 3 profiles: (AA), (BB) and (DD) on the residual anomalies (Figure 6 and Figure 7) of the intrusive bodies located on the Bipindi-Ebolowa I axis (C7 and G5), Eseka-Pouma axis (C14 and G8) and Bokito-Monatele axis (C18 and G11). On the AA, BB and DD profiles, 80 measurement points, 60 measurement points and 90 measurement points were taken respectively, all equidistant by 0.15 km. The upper end of each profile was chosen as a reference point for the calculation of distances. The geographical coordinates of these reference points are as follows: (10˚56'E, 3˚18'N) for profile AA, (10˚57'E, 3˚83'N) for profile BB and (11˚05'E, 4˚29'N) for profile DD.

Figures 8-10 show the gravimetric power spectrum as a function of wavenumber for the AA (Figure 8), BB (Figure 9) and DD (Figure 10) profiles of bodies (C7 and G5), (C14 and G8) and (C18 and G11) respectively. Each spectral curve shows two to three quantities which are the average interfaces depths of low, medium and high frequency respectively.

We obtain ($h_1 = 4.86$ km , $h_2 = 2.16$ km and $h_3 = 0.56$ km) for the AA profile of the C7 body and ($h_4 = 3.80$ km , $h_5 = 2.02$ km and $h_6 = 0.61$ km) for the same AA profile of the G5 body (Figure 8(a) and Figure 8(b)). These results

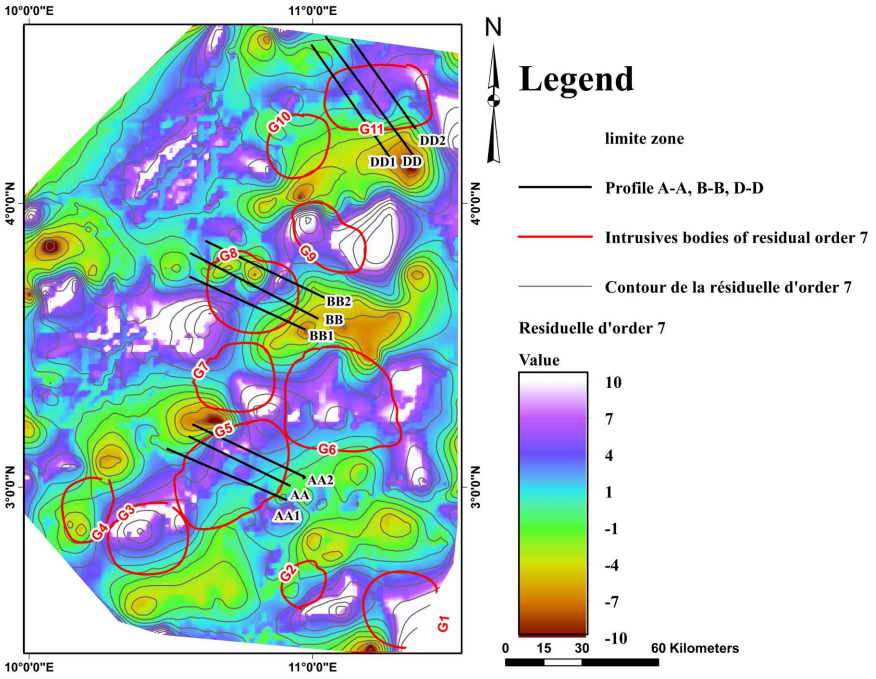

Figure 7. Overlay of the residual of order 7 on the intrusive bodies detected by the NSTD.

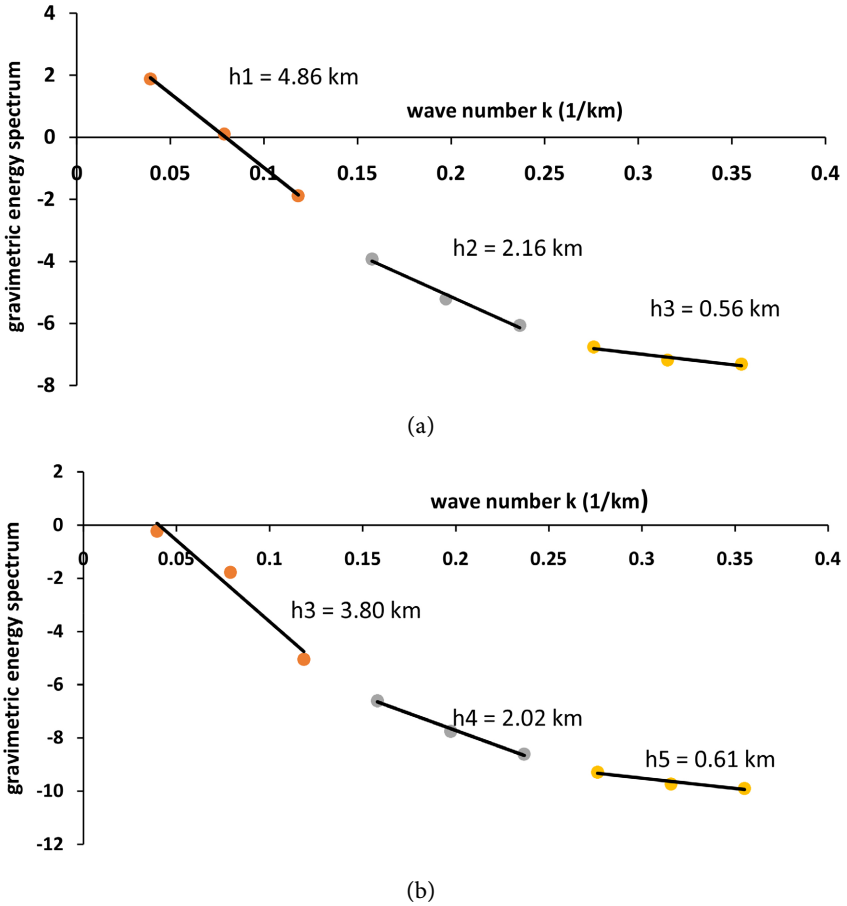

Figure 8. The spectral energy of the AA profile of the bodies obtained by NSTD for the: (a) first order residual (C7), (b) seventh order residual (G5).

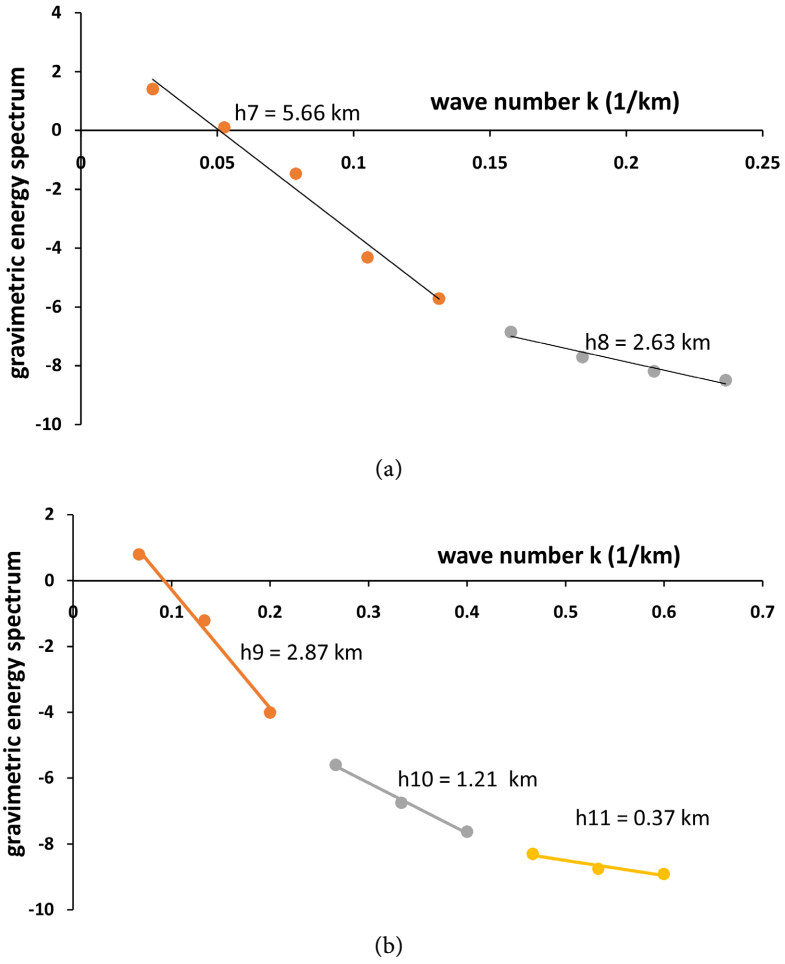

Figure 9. The spectral energy of the BB profile of the bodies obtained by NSTD for the: (a) 1st order residual (C14), (b) 7th order residual (G8).

show, taking into account the different uncertainties in the measurements and calculations, that the C7 and G5 intrusive bodies have practically the same roof depths (around 0.6 km). We can, therefore, deduce that C7 and G5, whose contours are correctly superimposed (**Figure 5**), merge into one and the same intrusive body. Finally, we can say that this intrusive body is positioned such that the different curvatures of the degree 7 polynomials have caused a suppression of the gravitational effect of about 1 km thickness of this body on the residual of order 7 from its base (we note a difference of about 1 km between the base depths h_1 and h_4).

Next, we obtain (**Figure 9(a)** and **Figure 9(b)**) for the BB profile of the C14 intrusive body ($h_7 = 5.66$ km , $h_8 = 2.63$ km) and for the same BB profile of the G8 body ($h_9 = 2.87$ km , $h_{10} = 1.21$ km and $h_{11} = 0.37$ km). Taking into account the different uncertainties in the measurements and calculations, the depth of the roof of C14 (2.63 km) is practically equal to the depth of the base of G8 (2.87 km), indicating that these are two different intrusive bodies located on the same vertical (their contours are correctly superimposed as shown in **Figure 5**), one (G8) above the other (C14).

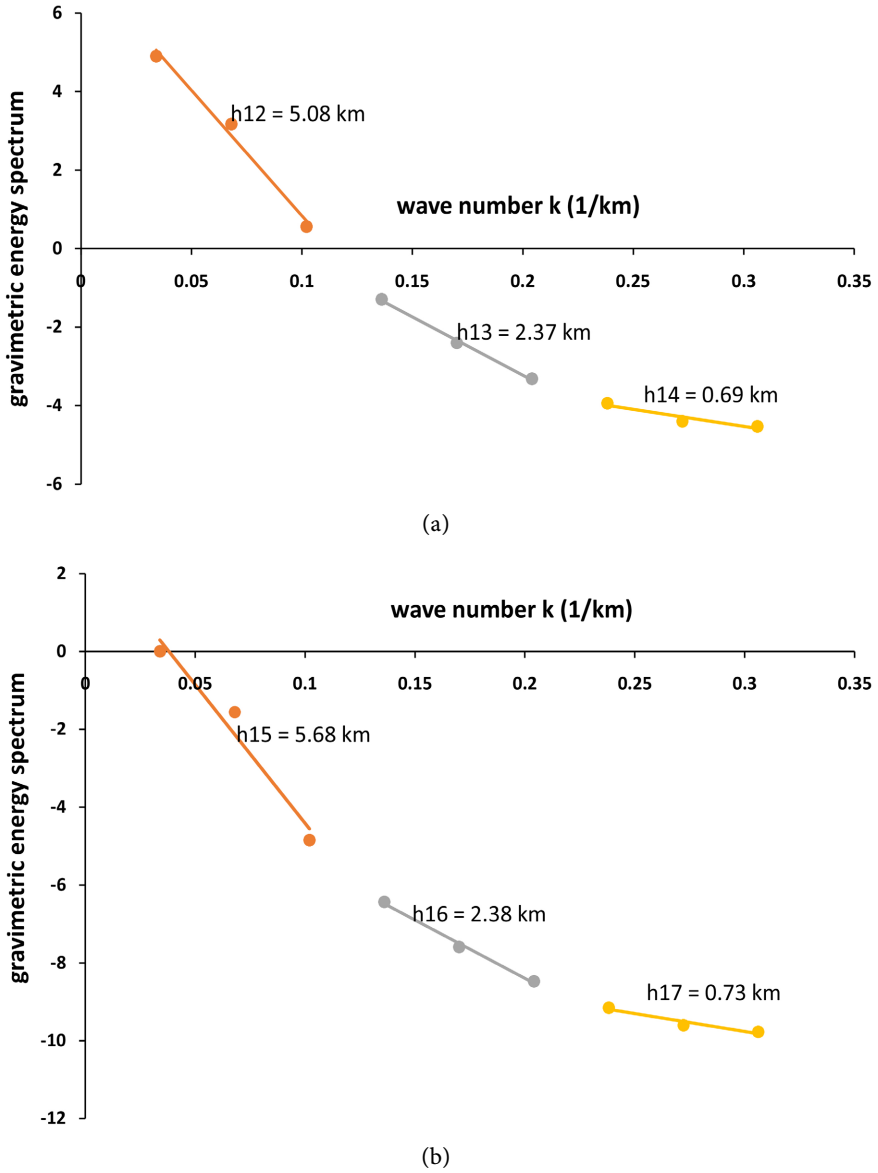

Figure 10. The spectral energy of the DD profile of the bodies obtained by NSTD for the: (a) 1st order residual (C18), (b) 7th order residual (G11).

Finally, we obtain (**Figure 10(a)** and **Figure 10(b)**) for the DD profile of the C18 intrusive body ($h_{12} = 5.08$ km , $h_{13} = 2.37$ km and $h_{14} = 0.69$ km) and for the same DD profile of the G11 body ($h_{15} = 5.68$ km , $h_{16} = 2.38$ km and $h_{17} = 0.73$ km). Taking into account the different uncertainties in the measurements and calculations, we see that the C18 and G11 intrusive bodies have practically the same roof depths (around 0.7 km). It thus appears that C18 and G11, whose contours are correctly superimposed (**Figure 5**), merge into one and the same intrusive body. Finally, we can say that this intrusive body is positioned such that the different curvatures of the polynomials of degree 7 have not caused any suppression of the gravitational effect of a part of this body on the residual of order 7 (we note well that the base depths h_{12} and h_{15} are practically equal).

5.5. Application of Inversion to Profile Data

To apply the inversion on real data, we chose the previous profiles (AA), (BB) and (DD) on the 7th order residual map with the same data that were used for the spectral analysis. An error with a standard deviation of 0.001 of its magnitude was assigned to the data. We subdivided the subsurface into 100 × 60 = 6000 cells, the length of each cell being inversely proportional to the length of the profile and the height inversely proportional to the total thickness of the layer. The inversion was made by considering a range of density contrast of the bedrock from [−0.22 to 0.73 g/cm^3]. This interval values is derived from the difference between the highest and lowest density rocks found in the study area and the average density of the earth's crust, which was taken as 2.67 g/cm^3 when calculating Bouguer's anomaly. These rocks are listed in **Table 1**.

To properly evaluate the anomaly located on the Bipindi-Ebolowa I, Eséka-Pouma and Bokito-Monatele axes, we took as input parameters, the profile data and as output condition the results of the spectral analysis. In running the inversion program, good results are obtained for density contrast values varying between 0.095 and 0.18 g/cm^3.

It can be seen in **Figure 11(a)** that the observed and calculated anomaly curves practically overlap. **Figure 11(b)** shows the density model recovered after inversion of the profile data (AA). It clearly represents the density distribution and in this case, the geometry of the surface of the present structure. To obtain this result we assumed a layer thickness of 8 km and a tolerance value of 0.3 km.

As can be seen from the results in **Figure 11(b)**, there is a variation in the base depth between [0.5 km; 3.7 km] with a tolerance value of 0.3 km; and a roof depth between approximately [0 km; 0.4 km].

Figure 12 shows a 3D view of the 2D profiles plotted on the G5 body. In **Figure 12**, it can be seen that the G5 body is deeper in the centre and at the left end of the structure. These results show that the intrusive body located on the Bipindi-Ebolowa I axis (G5) has an estimated density contrast of 0.12 g/cm^3.

It can be seen in **Figure 13(a)** that the curves of the observed anomaly and the calculated one practically overlap. To obtain this result we assumed a layer

Table 1. Densities of rocks found in the study area (Telford et al., 1976; Maurizot et al., 1986).

Types of Rocks	Density (g/cm^3)	Density Average (g/cm^3)	Types of Rocks	Density (g/cm^3)	Density Average (g/cm^3)
Amphibolite	2.9 - 3.04	2.96	Granodiorites	2.7 - 2.9	2.8
Dolerites	2.50 - 3.1	2.80	Granulites	2.78 - 3.37	3.1
Gneiss	2.6 - 3	2.80	Granites	2.5 - 2.7	2.6
Rhyolites	2.30 - 2.60	2.45	Peridotites	3.3 - 3.5	3.4
Charnockites	2.9 - 3.1	2.90	Schists	2.7 - 3.19	2.95
Basalts	2.98 - 3.30	3.14	Pyroxene	3.2 - 3.6	3.4

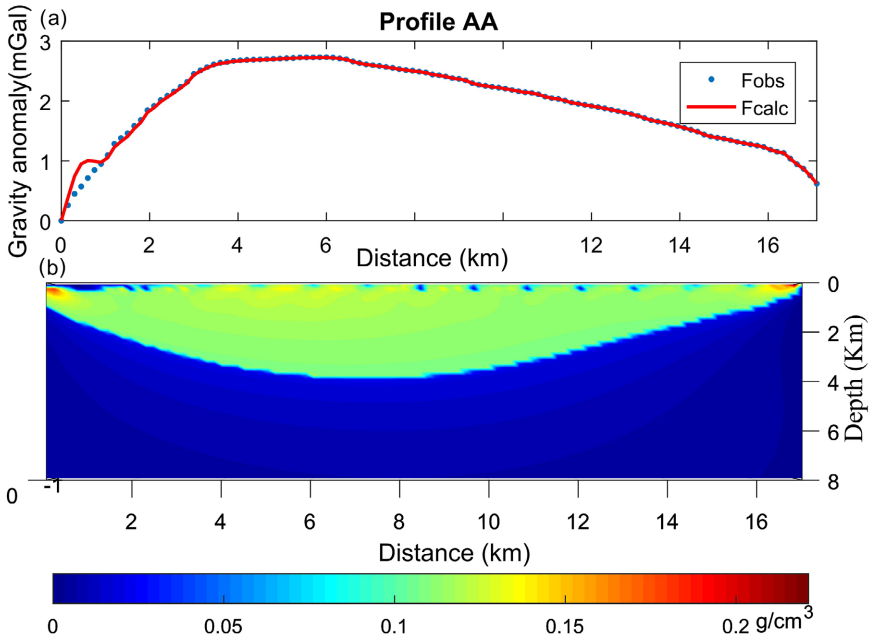

Figure 11. (a) Profile (AA) of gravity data; (b) Result of the inversion of the gravity data of the profile (AA) of the 7th order residual.

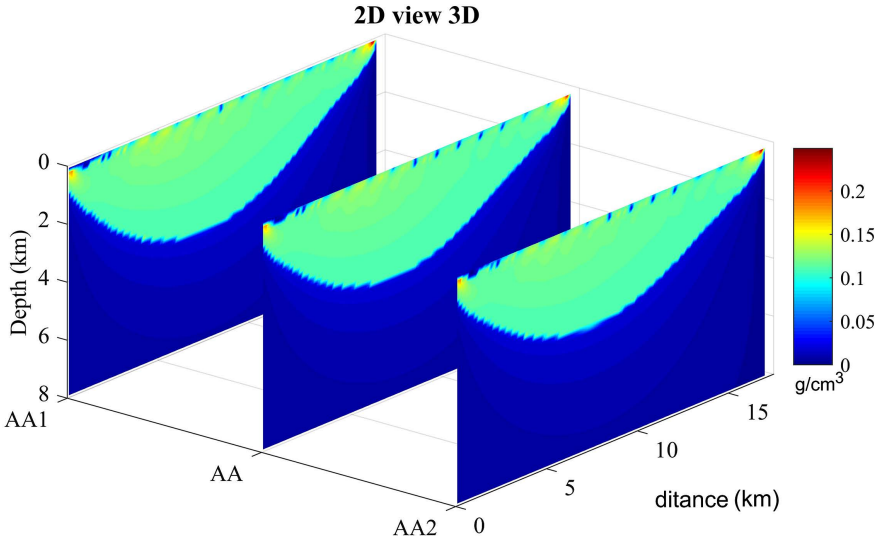

Figure 12. 3D view of the gravity data inversion of the 2D profiles (AA1, AA and AA2) of the 7th order residual.

thickness of 8 km and a tolerance value of 0.3 km. Figure 13(b) shows that the top of the structure is found to vary between [0 km; 0.3 km] of the earth's surface and its base is located between [1 km; 3.1 km].

Figure 14 shows a 3D view of the 2D profiles drawn on the G8 body. In Figure 14, it can be seen that the G8 body is deeper in the centre and at the right end of the structure. These results show that the anomaly located between Eseka and Pouma is due to an intrusive body (G8) whose density contrast is estimated at 0.13 g/cm^3.

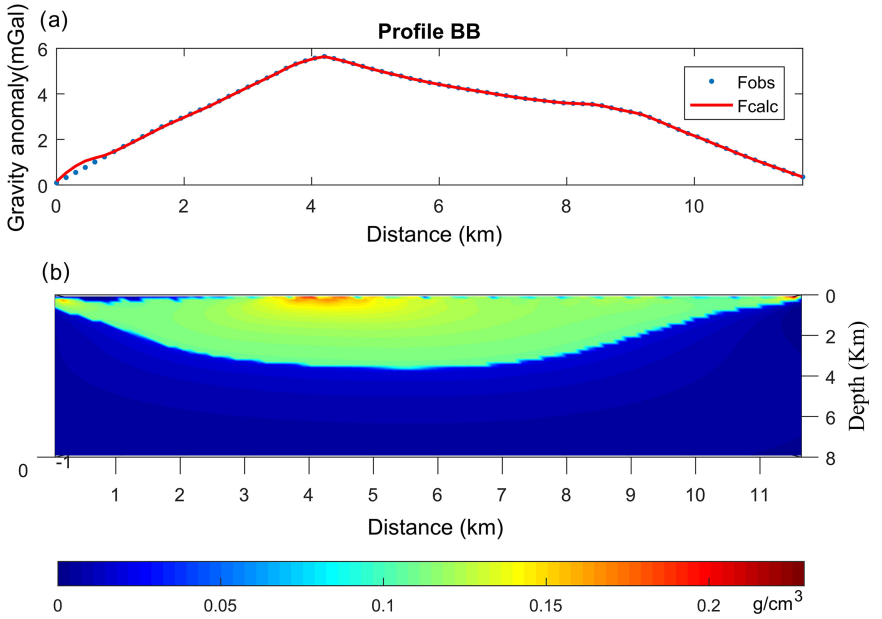

Figure 13. (a) Profile (BB) of gravity data; (b) Result of the inversion of the gravity data of profile (BB) of the 7th order residual.

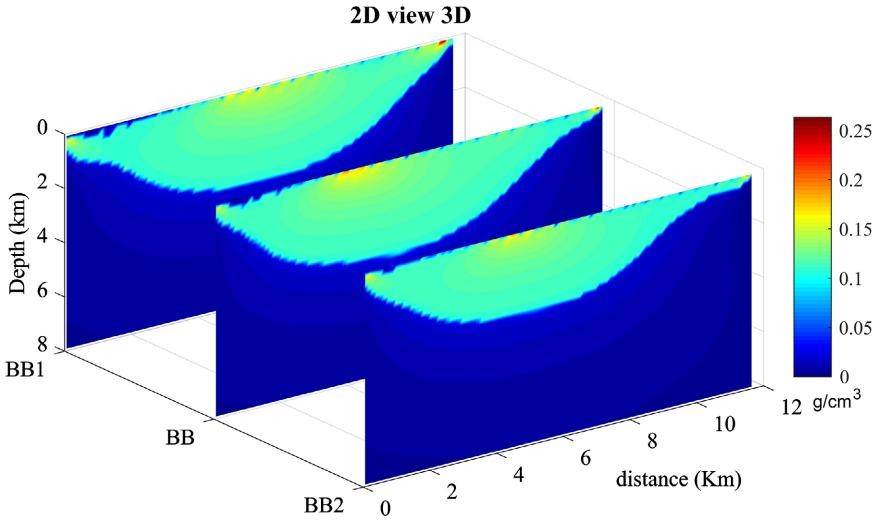

Figure 14. 3D view of the gravity data inversion of the 2D profiles (BB1, BB and BB2) of the 7th order residual.

It can be seen in Figure 15(a) that the curves of the observed anomaly and the calculated anomaly practically overlap. To obtain this result we assumed a layer thickness of 8 km and a tolerance value of 0.3 km. Figure 15(b) shows that the top of the structure is found to vary between [0 km; 0.3 km] of the earth's surface and its base is located between [1 km; 6 km].

Figure 16 shows a 3D view of the 2D profiles drawn on body G11. In Figure 16, it can be seen that the G11 body is deeper at the right end of the structure. These results show that the anomaly located between Bokito and Monatele is due to an intrusive body (G11) whose density contrast is estimated at 0.18 g/cm^3.

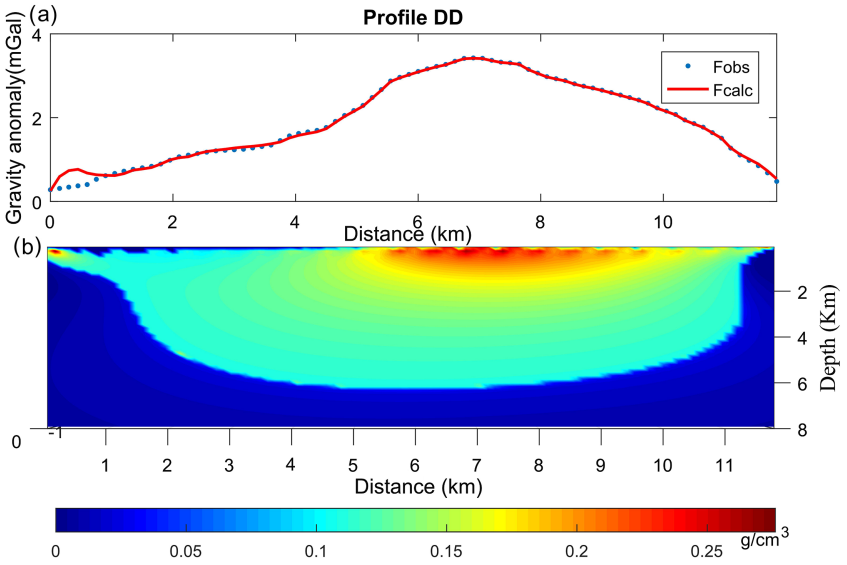

Figure 15. (a) Profile (DD) of severity data; (b) Result of the inversion of the severity data of the profile (DD) of the 7th order residual.

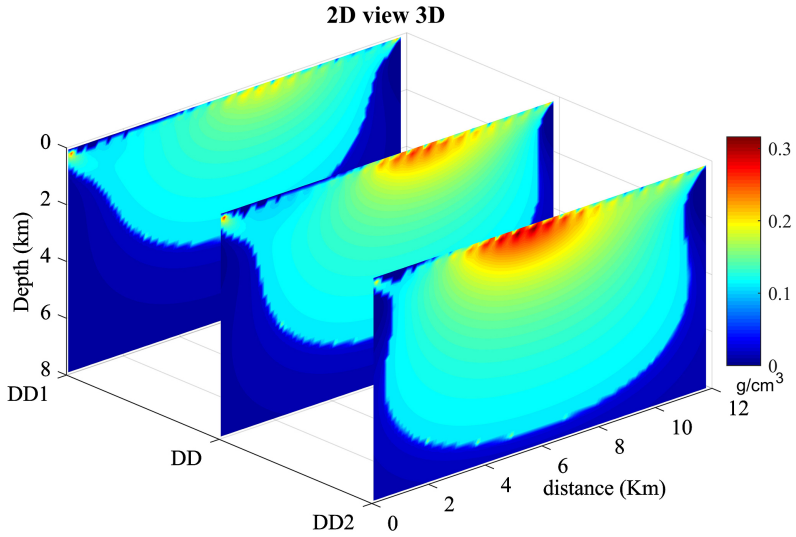

Figure 16. 3D view of the gravity data inversion of the 2D profiles (DD1, DD and DD2) of the 7th order residual.

6. Discussion

The application of NSTD allowed us to identify 18 intrusive bodies for the first-order residual and 11 for the seventh-order residual. Some of the intrusive bodies obtained in this study and quoted below are identifiable in the results of previous works. The intrusive body C6) of Bipindi (**Figure 5**) was characterised by Tchameni et al. (2001), Shang et al. (2004) and Owona et al. (2012). Later, Koumetio et al. (2014) proposed a 3D model of this body and found that its roof depth varies between 1 km and 2 km. The C5 and C13 intrusive bodies (**Figure 5**) of Kribi-Edea were characterised by Koumetio et al. (2012), who show that these bodies have a roof at about 1 km depth. We can also mention the Matomb

intrusive body (C16 of the first-order residual superimposed on G9 of the seventh-order residual) characterised by Koumetio et al. (2018), who found that the depth of its roof varies from 0.9 km to 3.2 km. These results clearly show that the structures detected by previous work and found in this study have a roof quite close to the Earth's surface.

In order to better analyse the map of intrusive bodies presented in **Figure 5**, we superimposed those of the 7th order residual on the geological and mineral resources map of Cameroon established by Toteu et al. (2008) to obtain **Figure 17**. This superposition allows us to see that several intrusive structures are located under different mineral deposit sites in the South West Cameroon area. Bodies G6 and G7 are located in areas where banded earth formations are found. The G5 body is in an environment where basaltic and ultra-basaltic magnetic deposits exist. The G9 bodies are superimposed on areas of alluvial-eluvial and beach sand deposits. The G5, G6 and G7 intrusive bodies are also found in an environment where garnet amphibolo-pyroxenites outcrop (**Figure 17**). Foucault and Raoult (2005) indicate that an amphibolite is an infrequent ultrabasic magmatic rock, essentially composed of amphibole and that pyroxenite is often used for pyroxenolite which is an ultrabasic magmatic rock composed essentially of pyroxene. They add that ultrabasic magmatic rocks are very rich in Mg, Fe and Ca. It appears that the new structures G5, G6 and G7 are of great interest for mining research. As the magma generally rises from the upper mantle at high temperatures, it can also be stated that these new intrusive bodies are in areas suitable for geothermal reservoir research.

The results of the spectral analysis (**Figure 8**) present the depths of the G5 body interfaces ($h_4 = 3.80$ km ; $h_5 = 2.02$ km and $h_6 = 0.61$ km); which are in agreement with those of **Figure 11(b)**, which presents, for G5, a density distribution with a roof that varies between [0 km; 0.4 km] and a base that varies between [0.5 km; 3.7 km] in depth. Indeed, with a tolerance value taken equal to 0.3 km, the depth of the roof of G5 can vary from 0 to 0.7 km, which is consistent with the value of about 0.6 km found by spectral analysis; It can also be stated that a continuous variation of the base depth from 0.5 km to 3.7 km would correspond to a structure that creates an anomaly equal to that of a body with a base at a constant depth of about 3.8 km and another interface at a constant depth of about 2 km that is due to a change in the lateral extent of the intrusive body. In **Figure 13(b)** the 2D density distribution of the G8 body is presented, its upper surface depth varies between [0 km; 0.3 km] and its base is located between [1 km; 3.1 km] depth, which is in agreement with the results (**Figure 9**) of the spectral analysis ($h_9 = 2.87$ km ; $h_{10} = 1.21$ km and $h_{11} = 0.37$ km). In **Figure 15(b)**, the 2D density distribution of body G11 is presented, its upper surface depth varies between [0 km; 0.3 km] and its base is located between [1 km; 6 km] depth, which is in agreement with the results (**Figure 10**) of the spectral analysis ($h_{15} = 5.68$ km ; $h_{16} = 2.38$ km and $h_{17} = 0.73$ km), taking into account the tolerance value of 0.3 km.

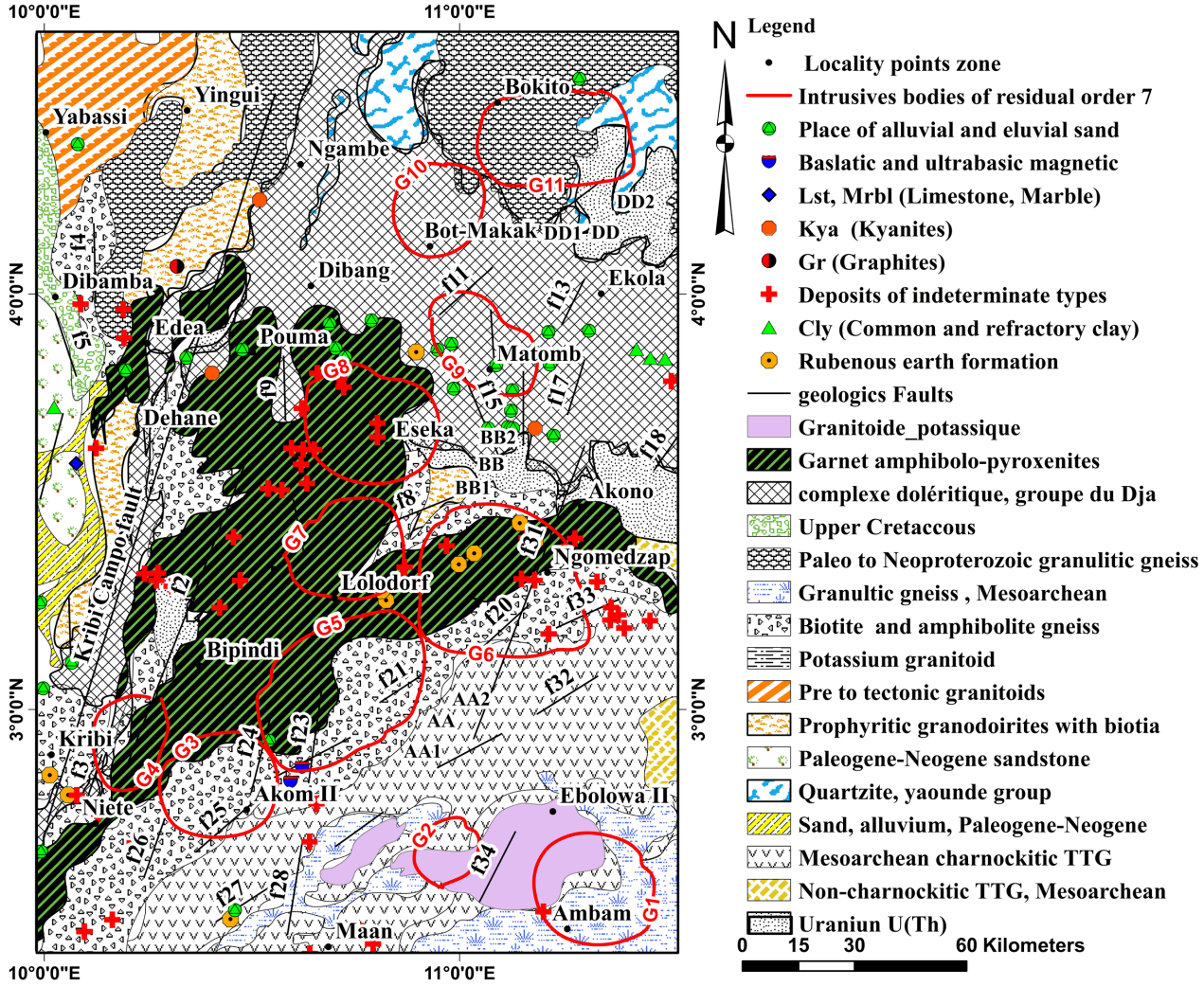

Figure 17. Geological and mineral resources map of Cameroon proposed by Toteu et al. (2008) modified, and superimposed on the intrusive bodies highlighted by the NSTD of the 7th order residual.

The density contrast values obtained by inversion (0.12, 0.13 and 0.18 g/cm^3) indicate that the intrusive bodies G5, G8 and G11 are denser than the surrounding rock, which leads them to create positive anomalies, invisible signs of infiltration of magmatic rocks at the surface (Kenfack et al., 2011). We also note that the superposition map of the residual of order 7 with the intrusive bodies (**Figure 7**) shows that many of these intrusive structures have created positive anomalies. The characterization of G5, G8 and G11 formations shows that the tops of most of these intrusive bodies are less than a kilometer deep, which makes them interesting for mining prospecting and for research of geothermal reservoirs since the magma which is at the origin of the establishment of these intrusive structures arrives with a high temperature while being rich in metallic ore.

Joel et al. (2022) identified geothermal reservoirs in an area that covers a southwestern part of our study area (it contains the localities of Bipindi, Nyete and Ma'an which are indicated in **Figure 1**, **Figures 4-7** and **Figure 17**) from

combined Landsat 8 and audio-magnetotelluric (AMT) data. They found that localities such as Nyete and Menve'ele (located east of Ma'an) with low electrical resistivity and high temperature are potential geothermal reservoirs. It can be seen on the map of the superposition of 7th order residual anomalies to the intrusive bodies detected by the NSTD (**Figure 7**) that there are strong positive anomalies in Nyete and east of Ma'an probably indicating the presence of near surface magmatic rocks. Also, shown in **Figure 7** is the G3 intrusive structure which must be the magma body that creates the strong positive anomaly in Nyete. For the area of east of Ma'an, the positive anomaly is circumscribed only at the boundary so that our gravity data could not clearly outline the source intrusive body by NSTD. The results of our study, therefore, corroborate those of Joel et al. (2022) with respect to the geothermal reservoir potentials in the area covering the localities of Bipindi, Nyete and Ma'an.

The Cameroon Volcanic Line (CVL) passing very close to the northern edge of the study area is a very important asset for the search for geothermal reservoirs. This zone, which has undergone several tectonic phenomena, allows the infiltration of water, which heats up in contact with magmatic rocks, producing geothermal water. This geothermal water circulates in granite and is enriched with a range of minerals (sodium chloride, dissolved gases) and some small radioactive elements such as radium, thorium, uranium, potassium and lead. The geothermal water is made up of these deposits, which are a source of minerals in the area. Some of these minerals can be seen on the mineral resources map in **Figure 17** (uranium, thorium, potassium granitoid), which appear as geothermal water deposits (Joel et al., 2022).

7. Conclusion

The combined application of indirect, inverse and normalized standard deviation methods on residual anomalies of gravity data from South-West Cameroon has allowed the identification of shallow intrusive structures present in this area. This study has thus improved the knowledge related to the interpretation of gravity data in order to characterise the near-surface intrusive bodies and analyse their mining and geothermal implications. The analysis of the maps obtained shows the presence of new intrusive bodies and those already highlighted by other authors in the area of South-West Cameroon. The spectral analysis method was used to estimate the depth of the roof and base of the intrusive bodies located on the Bipindi-Ebolowa I (G5), Eséka-Pouma (G8) and Bokito-Monatele (G11) axes, while the inverse method was used to estimate the range of variation in density contrasts due to these bodies. The study shows that many of these intrusive structures have created positive anomalies, which is an invisible sign of infiltration of magmatic rocks toward the surface. From the values of the depths obtained for G5, G8 and G11 formations, and by considering the values of the residual anomalies of order 7 at the level of the different intrusions, it appears that the tops of most of these intrusive bodies are less than a kilometer deep, which makes them interesting for mining prospecting and for research of geo-

thermal reservoirs. Finally, it was noted that the structures presented are in perfect correlation with previous work, and analysis led to the conclusion that new intrusive bodies, detected in the vicinity of the Cameroon Volcanic Line, are of great interest for mining and geothermal resources.

Acknowledgements

This work was carried out at the University of Dschang, Cameroon, as a part of the first author's Ph.D. studies. The authors thank IRD (Institut de Recherche pour le Développement) for providing gravity data used in this work. This paper benefits from the fruitful criticism and suggestions by the editor and anonymous reviewers, they are gratefully acknowledged.

Data Availability

The gravity data used to support the findings of this study were supplied by IRD (Institut de Recherche pour le Développement) under restriction to transmit it to third parties and hence cannot be made freely available. Requests for access to these data should be made to the corresponding author.

Conflicts of Interest

The authors declare no conflicts of interest regarding the publication of this paper.

References

Blakely, R. J., & Simpson, R. W. (1986). Approximating Edges of Source Bodies from Magnetic or Gravity Anomalies. *Geophysics, 51,* 1494-1498. https://doi.org/10.1190/1.1442197

Bonda, B. M. M., Vishiti, A., Joel, M. S., Constantin, B. E., François, N. N. G., & Jacques, E. (2022). Microchemical Fingerprint of Magnetite Bearing Iron Ore Deposit from the Sanaga Prospect, Southern Cameroon: Assessment of Iron Ore-forming Conditions. *Journal of Geosciences, 10,* 65-73.

Bouyo Houketchang, M., Penaye, J., Mouri, H., & Toteu, S. F. (2019). Eclogite Facies Metabasites From the Paleoproterozoic Nyong Group, SW Cameroon: Mineralogical Evidence and Implications for a High-Pressure Metamorphism Related to a Subduction Zone at the NW Margin of the Archean Congo Craton. *Journal of African Earth Science, 149,* 215-234. https://doi.org/10.1016/j.jafrearsci.2018.08.010

Chakravarthi, V., Raghuram, H. M., & Singh, S. B. (2002). 3-D Forward Gravity Modeling of Basement Interfaces Above Which the Density Contrast Varies Continuously with Depth. *Computers & Geosciences., 28,* 53-57. https://doi.org/10.1016/S0098-3004(01)00080-2

Collignon, F. (1968). *Gravimétrie et reconnaissance de la République Fédérale du Cameroun.* ORSTOM.

Cooper, G. R., J., & Cowan, D. R. (2008). Edge Enhancement of Potential-Filed Data Using Normalized Statistics. *Geophysics, 73,* H1-H4. https://doi.org/10.1190/1.2837309

Dimitriadis, K., Tselentis, G. A., & Thanassoulas, K. (1987). A BASIC Program for 2D Spectral Analysis of Gravity Data and Source Depth Estimation. *Computers and Geosciences,*

13, 549-560. https://doi.org/10.1016/0098-3004(87)90056-2

Feybesse, J. L., Johan, V., Triboulet, V., Guerrot, C., Mayaka-Mikolo, F., Bouchot, V., & Eko, N. J. (1998). The West Central African Belt: A Model of 2.5-2.0 Ga Accretion and Two-Phase Orogenic Evolution. *Precambrian Research, 87,* 161-216. https://doi.org/10.1016/S0301-9268(97)00053-3

Fofie, K. A. D., Koumetio, F., Kenfack, J. V., & Yemele, D. (2019). Lineament Characteristics Using Gravity Data in the Garoua Zone, North Cameroon: Natural Risks Implications. *Earth and Planetary Physics, 3,* 33-44. https://doi.org/10.26464/epp2019009

Foucault, A., & Raoult, J. F. (2005). *Dictionnaire de géologie* (352 p.). Dunod.

Gantar, C., Honkasalo, T., McConnell, R. K., Tanner, J. G., Szabo, B., Uotila, U., & Whalen, C. T. (1971). *The International Gravity Standardization: Net 1971* (IGSN 71) (192 p.). Bureau Central de l'Association Internationale de Geodésie.

Joel, P. K., Louise-Clotilde, O. A. M., Evariste, N., Nfor, N., Malquaire, K. P. R., & Philippe, N. N. (2022). Identification of Geothermal Reservoirs in South Cameroon from a Combined Landsat 8 and AMT Data. *International Journal of Geophysics, 2022,* Article ID: 1324766. https://doi.org/10.1155/2022/1324766

Kenfack, J. V., Tadjou, J. M., Kamguia, J., Tabod, T. C., & Bekoa, A. (2011). Gravity Interpretation of the Cameroon Mountain (West Central Africa). Based on the New and Existing Data. *International Journal of Geosciences, 2,* 513-522. https://doi.org/10.4236/ijg.2011.24054

Kenyo, B., Koumetio, F., Kwekam, M., & Kengni, L. (2023). Characteristics of Lineaments Using Gravity Data in the Eastern Cameroon: Structural, Hydrogeological and Natural Risks Implications. *Journal of African Earth Sciences, 202,* Article ID: 104886. https://doi.org/10.1016/j.jafrearsci.2023.104886

Kouankap, N. G. D., Njiosseu, T. E. L., Takodjou, W. J. D., Kamguia, W. B. ., Afahnwie, N. A., Fomena, T. H., & Folah, M. C. L. (2018). Petro-Structural Characterization of Bonguen Area, Nyong Series, Cameroon: Insight into the Northern Extension of Kribi-Campo Shear Zone, West *Ethiopia. Earth Sciences, 7,* 236-241. https://doi.org/10.11648/j.earth.20180705.15

Koumetio, F. (2004). *Contribution géophysique par méthode gravimétrique à l'étude des structures profondes de la marge occidentale du craton du Congo dans la région de Kribi (Cameroun)* (110 p.). Ph.D. Thesis, Université de Yaounde I.

Koumetio, F. (2017). *Investigation géophysique par méthodes gravimétriques dans la région du Sud-ouest Cameroun: Implications structurales et tectoniques(Cameroun)* (180 p.). Ph.D. Thesis, Université de Yaounde I.

Koumetio, F., Njomo, D., Tabod, C. T., Noutchogwe Tatchum, C., & Manguelle-Dicoum, E. (2012). Structural Interpretation of Gravity Anomalies from the Kribi-Edea Zone, South Cameroon: A Case Study. *Journal of Geophysics and Engineering, 9,* 664-673. https://doi.org/10.1088/1742-2132/9/6/664

Koumetio, F., Njomo, D., Tatchum Noutchogwe, C., Ndoh Ndikum, E., Nguiya, S., & Kamga Tokam, A. P. (2019). Choice of Suitable Regional and Residual Gravity Maps, the Case of the South-West Cameroon Zone. *Earth and Planetary Physics, 3,* 26-32. https://doi.org/10.26464/epp2019004

Koumetio, F., Njomo, D., Tatchum, C. N., Tokam, A. P. K., Tabod, T. C., & Manguelle-Dicoum, E. (2014). Interpretation of Gravity Anomalies by Multi-Scale Evaluation of Maxima of Gradients and 3D Modelling in Bipindi Region (South-West Cameroon). *International Journal of Geosciences, 5,* 1415-1425. https://doi.org/10.4236/ijg.2014.512115

Koumetio, F., Noutchogwe, C. T., Nouayou, R., Ndikum, E., Wandji, V. J. T., & Dika, A.

(2018). Interpretation of Gravity Anomaly in the Area of Matomb (Center Cameroon) Using Direct, Indirect and Inverse Methods. *International Journal of Research and Innovations in Earth Science, 5,* 106-111.

Last, B. J., & Kubik, K. (1983). Compact gravity inversion. *Geophysics, 48,* 713-721. https://doi.org/10.1190/1.1441501

Loose, D., & Schenk, V. (2018). 2.09 Ga Old Eclogites in the Eburnian-Transamazonian Orogen of Southern Cameroon: Significance for Palaeoproterozoic Plate Tectonic. *Precambrian Research, 304,* 1-11. https://doi.org/10.1016/j.precamres.2017.10.018

Maurizot, P., Abessolo, A., Feybesse, J. L., Johan, V., & Lecomte, P. (1986). *Etude et prospection minière dusud-ouest Cameroun. Synthèse des travaux de 1978 à 1985* (274 p.). BRGM.

Minyem, D., & Nedelec, A. (1990). Origin and Evolution of the Eseka Gneisses (Cameroon) Archean TTG Reworked in the Panafrican Mobile Belt. In *15th Colloquium of African Geology* (pp. 21-24). Occasional Publication.

Mvodo, H., Ganno, S., Kouankap Nono, G. D., Fossi, D. H., Nga Essomba, P. E., Tankwa, M. N. et al. (2022). Petrogenesis, LA-ICP-MS Zircon U-Pb Geochronology and Geodynamic Implications of the Kribi Metavolcanic Rocks, Nyong Group, Congo Craton. *Acta Geochimica, 41,* 470-495. https://doi.org/10.1007/s11631-022-00533-2

Nedelec, A., Nsifa, E. N., & Martin, H. (1990). Major and Trace Element Geochemistry of the Archean Ntem Plutonic Complex (South Cameroon): Petrogenesis and Crustal Evolution. *Precambrian Research, 47,* 35-50. https://doi.org/10.1016/0301-9268(90)90029-P

Nga Essomba, T. P., Ganno, S., Tanko Njiosseu, E. L., Ndema Mbongue, J. L., Kamguia, Woguia, B., Soh Tamehe, L. et al. (2020). Geochemical Constraints on the Origin and Tectonic Setting of the Serpentinized Peridotites from the Paleoproterozoic Nyong Series, Eseka Area, SW Cameroon. *Acta Geochimica, 39,* 404-422. https://doi.org/10.1007/s11631-019-00368-4

Ngako, V., Affaton, P., Nnange, J. M., & Njanko, T. (2003). Pan-African Tectonic Evolution in Central and Southern Cameroon: Transpression and Transtension during Sinistral Shear Movements. *Journal of African Earth Sciences, 36,* 207-214. https://doi.org/10.1016/S0899-5362(03)00023-X

Nsifa, E. N. (2005). *Agmatisme et évolution géodynamique de l'Archéen au Protérozoïque de la bordure nordouest du craton du Congo (complexe du Ntem) au Sud-Ouest Cameroun* (248 p.). Ph.D. Thesis, Université de Yaounde I.

Nzenti, J. P. (1998). Neoproterozoic Alkaline Meta-Igneous Rocks from the Pan-African North Equatorial Fold Bel (Yaounde, Cameroon): Biotitites and Magnetite Rich Pyroxenites. *Journal of African Earth Sciences, 26,* 37-47. https://doi.org/10.1016/S0899-5362(97)00135-8

Nzenti, J. P., Abaga, A., Suh, C. E., & Nzolang, C. (2011). Petrogenesis of Peraluminous Magmas from the Akum-Bamenda Massif, Pan-African Fold Belt, Cameroon. *International Geology Review, 53,* 1121-1149. https://doi.org/10.1080/00206810903442402

Owona Angue, M. L. C., Nguiya, S., Nouayou, R., Tokam Kamga, A. P., & Manguelle-Dicoum, E. (2011). Geophysical Investigation of the Transition Zone between the Congo Craton and the Kribi-Campo Sedimentary Basin (Southwestern Cameroon). *South African Journal of Geology, 114,* 145-158. https://doi.org/10.2113/gssajg.114.2.145

Owona, S., Mvondo Ondoa, J., Tichomirowa, M., Ratschbacher, L., Tchoua, M. F., & Ekodeck, G. E. (2012). New $^{207}Pb/^{206}Pb$-Zr Minimum Evaporation, Metamorphic $^{87}Rb/^{86}Sr$-

WR-Bt Ages and Tectonic Imprints in the Archean So'o Group (Ntem Complex/Congo Craton, SW Cameroon). *Global Journal of Geological Sciences, 10,* 37-46.

Owona, S., Ratschbacher, L., Nsangou Ngapna, M., Gulzar, A. M., Mvondo Ondoa, J., & Ekodeck, G. E. (2021a). New U-Pb Zircon Ages of Nyong Complex Meta-Plutonites: Implications for the Eburnean/Trans-Amazonian Orogeny in Southwestern Cameroon (Central Africa). *Geological Journal, 56,* 1741-1755. https://doi.org/10.1002/gj.4022

Owona, S., Ratschbacher, L., Nsangou Ngapna, M., Gulzar, A. M., Mvondo Ondoa, J., & Ekodeck, G. E. (2021b). How Diverse is the Source? Age, Provenance, Reworking, and Overprint of Precambrian Meta-Sedimentary Rocks of West Gondwana, Cameroon, from Zircon U-Pb Geochronology. *Precambrian Research, 359,* 106-220. https://doi.org/10.1016/j.precamres.2021.106220

Owono, F. M. (2010). *Surrection cénozoïque de l'Ouest de l'Afrique à partir de deux exemples: Le plateau sudnamibien et la marge nord-camerounaise* (327 p.). Ph.D. Thesis, Université Rennes 1.

Pirttijärvi, M. (2009). *Fourpot* (34 p.). User's Guide, University of Oulu.

Poudjom-Djomani, Y. H., Boukeke, D. B., Legeley-Padovani, A., Nnange, J. M., Ateba, B., Albouy, Y., & Fairhead, J. D. (1996). *Levés gravimétriques de reconnaissance du Cameroun.* ORSTOM.

Radhakrishna, I. V., & Krishnamacharyulu, S. K. G. (1990). Polyfit: A Fortran 77 Program to Fit a Polynomial of Any Order to Potential Field Anomalies. *Journal of the Association of Exploration Geophysicists, 11,* 99-105. https://www.semanticscholar.org

Shanel, S. S. A. D., Djibril, K. N. G., Hermine, M., Sayom, P. N., Brice, K. W., & Paul, N. J. (2022). Petrography and Geophysical Characterization of the Newly Discovered Iron Ore Deposit in Makoure (Bidou-East), Nyong Group, South Cameroon. *Results in Geophysical Sciences, 12,* Article ID: 100050. https://ssrn.com/abstract=4214265 https://doi.org/10.1016/j.ringps.2022.100050

Shang, C. K., Wolfgang, S., Muharrem, S., Funken, C., & Mvondo Ondoa, J. (2004). Zircon Pb-Pband U-Pb Systematics of TTG Rocks in the Congo Craton: Constraints on Crust Formation, Magmatism, and Pan-African Lead Loss. *Bulletin of Geosciences, 79,* 205-219.

Spector, A., & Grant, F. (1970). Statistical Models for Interpreting Aeromagnetic Data. *Geophysics, 35,* 293-302. https://doi.org/10.1190/1.1440092

Tabod, C. T. (1991). *Seismological Studies of the Cameroon Volcanic Line in West Africa* (181 p.). Ph.D. Thesis, University of Leeds.

Tchameni, R. (1997). *Géochimie et Géochronologie des formations de l'Archéen et du Paléoprotérozoïque du Sud Cameroun (groupe du Ntem, craton du Congo)* (356 p.). Ph.D. Thesis, Université d'Orléans.

Tchameni, R., Mezger, K., Nsifa, N. E., & Pouclet, A. (2001). Crustal Origin of Early Proterozoic Syenites in the Congo Craton (Ntem Complex), South Cameroon. *Lithos, 57,* 23-42. https://doi.org/10.1016/S0024-4937(00)00072-4

Tchameni, R., Pouclet, A., Penaye, J., Ganwa, A. A., & Toteu, S. F. (2006). Petrography and Geochemistry of the Ngaoundéré Pan-African Granitoids in Central North Cameroon: Implications for Their Sources and Geological Setting. *Journal African Earth Sciences, 44,* 511-529. https://doi.org/10.1016/j.jafrearsci.2005.11.017

Telford, W. M., Geldart, L. P., & Keys, D. A. (1976). *Applied Geophysics* (pp. 24-26). Cambridge University Press.

Tokam, K. A. P. (2010). *Crustal Structure Beneath Cameroon Deduced from the Joint Inversion of Rayleigh Wave Group Velocities and Receiver Functions* (132 p.). Ph.D. Thesis, Université de Yaoundé I.

Toteu, S. F., Penaye, J., Deschamp, Y., Maldan, L., Nyama, A. B., Bouyo, H. M. et al. (2008). Géologie et ressources minérales du Cameroun. In *33rd International Geological Congress* (pp. 9-13).

Vigneresse, J. L. (1990). Use and Misuse of Geophysical Data to Determine the Shape at Depth of Granitic Intrusions. *Geological Journal, 25,* 249-260. https://doi.org/10.1002/gj.3350250308

Zewge, A., Lewi, E., & Midekso. (2011). Design and Implementation of Forward and Inverse Gravity Modeling Tool. *East African Journal of Sciences, 5,* 83-88.